

Pressure-induced superconductivity in quasi-one-dimensional semimetal Ta₂PdSe₆

Haiyang Yang,^{1,2} Yonghui Zhou,^{1,*} Liangyu Li,^{1,2} Zheng Chen,^{1,2} Zhuyi Zhang,^{1,2}
Shuyang Wang,^{1,2} Jing Wang,^{1,2} Xuliang Chen,¹ Chao An,³ Ying Zhou,³ Min Zhang,³
Ranran Zhang,¹ Xiangde Zhu,¹ Lili Zhang,⁴ Xiaoping Yang,^{1,*} and Zhaorong Yang^{1,3,*}

¹*Anhui Key Laboratory of Condensed Matter Physics at Extreme Conditions, High Magnetic
Field Laboratory, HFIPS, Chinese Academy of Sciences, Hefei 230031, China*

²*Science Island Branch of Graduate School, University of Science and Technology of China,
Hefei 230026, China*

³*Institutes of Physical Science and Information Technology, Anhui University, Hefei 230601,
China*

⁴*Shanghai Synchrotron Radiation Facility, Shanghai Advanced Research Institute, Chinese
Academy of Sciences, Shanghai 201204, China*

*Corresponding authors.

yhzhou@hmfl.ac.cn;

xpyang@hmfl.ac.cn;

zryang@issp.ac.cn

Abstract

Here we report the discovery of pressure-induced superconductivity in quasi-one-dimensional Ta_2PdSe_6 , through a combination of electrical transport, synchrotron x-ray diffraction (XRD), and theoretical calculations. Our transport measurements show that the superconductivity appears at a critical pressure $P_c \sim 18.3$ GPa and is robust upon further compression up to 62.6 GPa. The estimated upper critical field $\mu_0 H_{c2}(0)$ in the pressurized Ta_2PdSe_6 is much lower than Pauli limiting field, in contrast to the case in its isostructural analogs $\text{M}_2\text{Pd}_x\text{X}_5$ ($\text{M} = \text{Nb}, \text{Ta}$; $\text{X} = \text{S}, \text{Se}$). Concomitant with the occurrence of superconductivity, anomalies in pressure dependent transport properties are observed, including sign reversal of Hall coefficient, abnormally enhanced resistance, and dramatically suppressed magnetoresistance. Meanwhile, room-temperature synchrotron X-ray diffraction experiments reveal the stability of the pristine monoclinic structure (space group $C2/m$) upon compression. Combined with the density functional theory calculations, we argue that a pressure-induced Lifshitz transition could be the electronic origin of the emergent superconductivity in Ta_2PdSe_6 .

I. INTRODUCTION

Low-dimensional transition metal chalcogenides (TMC) are an emerging class of materials with properties that make them highly attractive for fundamental studies of novel physical phenomena, and for potential applications in electronics and optoelectronics [1-5]. Among them, quasi-one-dimensional (quasi-1D) $M_2Pd_xX_5$ ($M = Nb, Ta$; $X = S, Se$) and $Ta_4Pd_3Te_{16}$ have been paid special attention, mainly focusing on their unusual superconductivity. On one hand, $M_2Pd_xX_5$ superconductors were reported to display an upper critical magnetic field H_{c2} that is far beyond the Pauli paramagnetic limit [6-9]. The extremely large H_{c2} could be ascribed to strong spin-orbit coupling, multi-band effect, or even spin-triplet pairing [6-11]. On the other hand, associated with their quasi-1D character, $M_2Pd_xX_5$ and $Ta_4Pd_3Te_{16}$ superconductors can be easily fabricated into nanowires, nanostrips and long fibers, leading to emergent phenomena such as size-controlled superconductor-insulator transition, and magnetic-field-induced reentrance of superconductivity [12-15]. Moreover, quasi-1D materials could have a strong tendency to form a charge density wave (CDW). For example, $Ta_4Pd_3Te_{16}$ was reported to display coexistence and interesting interplay between CDW and superconductivity [16-20].

As isostructural analogs of M_2PdX_5 ($M = Nb, Ta$; $X = S, Se$), Ta_2PdX_6 crystallize in monoclinic structure with the same space group $C2/m$ [21]. For example, Ta_2PdSe_6 features a layered structure oriented parallel to the plane $(20\bar{1})$, As shown in Fig. 1(a). The layer is composed of $PdSe_4$ quadrilaterals and $TaSe_7$ polyhedra. The only difference between M_2PdX_5 and Ta_2PdX_6 is that face-shared TaX_7 instead of TaX_6 prisms form the 1D chains along b -axis in Ta_2PdX_6 . Since Ta_2PdX_6 have the very similar crystal structure as M_2PdX_5 , it can be expected that Ta_2PdX_6 are also superconducting. Unfortunately, so far there is no definite experimental evidence to support for the superconductivity in Ta_2PdX_6 [22,23]. Instead, Ta_2PdX_6 have been studied as photoelectric and thermoelectric materials. For example, few-layer Ta_2PdS_6 was reported to exhibit excellent optoelectronic performances such as ultrahigh photoresponsivity and high photoconductivity [24]. Bulk Ta_2PdSe_6 was reported to host a giant Peltier conductivity and a large power factor at 300 K [25,26], and theoretically predicted to be a topological nodal-line semimetal candidate [27].

It is well known that pressure as an effective control parameter can systematically tune lattice structures and the corresponding electronic states. In this work, we show

that Ta₂PdSe₆ can be driven into a superconductor under high pressure by electrical transport and synchrotron X-ray diffraction (XRD) measurements. The emergence of superconductivity at a critical pressure $P_c \sim 18.3$ GPa does not involve a structural transition, but is accompanied by abnormal evolution of normal state transport properties. Combining density functional theory (DFT) calculations and transport measurements, we conclude that a pressure-induced Lifshitz transition could be the electronic origin of the emergent superconductivity in Ta₂PdSe₆. Moreover, the H_{c2} in the superconducting Ta₂PdSe₆ is much lower than the Pauli limiting field, which is different from that in M₂PdX₅ (M = Nb, Ta; X = S, Se).

II. EXPERIMENTAL DETAILS & METHODS

Ta₂PdSe₆ single crystals were grown via chemical vapor transport method [25]. Stoichiometric amounts of high purity Ta, Pd, and Se with a weight of 0.5 g and 2 mg/cm³ of iodide were mixed thoroughly and then sealed in a quartz tube with a low vacuum pressure of $\leq 10^{-3}$ Pa. The tube was heated in a horizontal tube furnace with a temperature gradient of 120°C between 800°C and 680°C for one week. The obtained high-quality single crystals are shiny with the needle shape, as seen in the inset of Fig. 1(b). Room-temperature XRD patterns of single crystal were obtained with Cu K_α radiation ($\lambda = 1.5406$ Å) using a Rigaku X-ray diffractometer (Miniflex-600). It indicates that the (20 $\bar{1}$) plane is a natural cleavage facet. The atomic proportion of crystal was Ta_{2.1}PdSe_{5.9}, extracting from energy dispersive X-ray spectroscopy (EDXS, Helios Nanolab 600i, FEI) with area-scanning mode. The ambient pressure electrical transport measurements were performed in a physical property measurement system (PPMS, Quantum Design). Transport measurements were conducted along the b -axis of single crystal with a standard four-probe configuration, as shown in Fig. 1(d). The R - T curve is rather smooth and has no sharp anomaly, suggesting the absence of CDW transition in Ta₂PdSe₆. The sample exhibits a metallic behavior with a residual resistance ratio ($RRR = R_{300K}/R_{2K}$) of 1136.

High-pressure transport experiments were conducted in a screw-pressure-type diamond anvil cell made of CuBe alloy with a pair of anvil culets of 200 μ m. The low-temperature electrical transport measurements were carried out in a homemade multifunctional measurement system (1.8-300 K, JANIS Research Company Inc.; 0-9 T, Cryomagnetics Inc.), while an additional He3 insert (with temperatures down to 0.45

K) provided the ultra-low temperature environment. In run 1 and run 2, five-probe resistance and Hall effect measurements were performed by sweeping the magnetic field from -5 to $+5$ T perpendicular to $(20\bar{1})$ plane with a steady current along the b axis. A mixture of epoxy and fine cubic boron nitride powder was compressed firmly to insulate the electrodes from the T301 stainless steel gasket. Then, a hole of $130\ \mu\text{m}$ in diameter was drilled in the center of the pit, further filled with soft NaCl fine powder as the pressure-transmitting medium. A single crystal with dimensions of $\sim 70 \times 20 \times 10\ \mu\text{m}^3$ was loaded together with some ruby powder. Platinum foil with a thickness of $5\ \mu\text{m}$ was used for the electrodes. To detect the conductivity under an ultra-low temperature environment, a new round of electrical transport experiments was conducted with a standard four-probe configuration in run 3. The magnetic field orientation was consistent with runs 1 and run 2. The samples used in runs 1, run 2 and run3 are different pieces of single crystals from the same batch. High-pressure angle-dispersive synchrotron XRD experiments were carried out at room temperature with Ta_2PdSe_6 powder crushed from single crystals, at the beamline BL15U1 of the Shanghai Synchrotron Radiation Facility (SSRF) ($\lambda = 0.6199\ \text{\AA}$). The diamonds with culet size of $300\ \mu\text{m}$ and T301 stainless steel gasket were used. Daphne 7373 was used as the transmitting medium. A Mar345 image plate was used to record 2D diffraction patterns. The Dioptas [28] program was used for image integration, and the XRD patterns were fitted using the RIETICA [29] program with the Le Bail method. The pressure values for all of the above experiments were determined by the ruby fluorescence method at room temperature [30].

Electronic band structure and the Hellmann-Feynman force under different pressure were calculated by using the Vienna ab initio Simulation Package (VASP) [31,32] within the framework of generalized gradient approximation (GGA) (Perdew-Burke-Ernzerhof exchange functional) [33] and the modified Becke-Johnson (MBJ) exchange potential [34]. Spin-orbit coupling (SOC) for all elements was treated by a second-variation method. The ion-electron interaction was modeled by the projector augmented wave (PAW) method [35,36] with a uniform energy cutoff of 520 eV. Spacing between k points was $0.02\ \text{\AA}^{-1}$. The geometry structures were optimized by employing the conjugate gradient technique, and in the final geometry, no force on the atoms exceeded $0.001\ \text{eV/\AA}$. The phonon vibrational spectrum is investigated by using the finite displacement method implemented in Phonopy package [37]. In Fig. S1, GGA+SOC

and GGA+MBJ+SOC band structures at 0 GPa are plotted. Our GGA+SOC band structure in Fig. S1(a) is consistent with that in Ref. [26]. The introduction of the MBJ potential in Fig. S1(b) further corrects the band structures and yields band gaps with similar accuracy to the hybrid functional results.

III. RESULTS AND DISCUSSION

Figure 2 shows selected resistance-temperature $R(T)$ curves in the pressure range from 1.0 to 62.6 GPa. As shown in Fig. 2(a), the $R(T)$ curve at 1.0 GPa shares a similar metallic behavior with the case of ambient pressure. Below 12.8 GPa, Ta₂PdSe₆ remains metallic, and the resistance change slightly with increasing pressure. At 15.3 GPa, the $R(T)$ curve is shifted upward evidently. Upon further compression to 18.3 GPa, a tiny resistance drop is marked by the arrow at ~ 1.9 K, a temperature just above 1.8 K, the lowest temperature of the experiment in run 1. Such a drop becomes more and more pronounced at higher pressures, and the zero resistance is finally achieved above 38.1 GPa [see Fig. 2(b)], signaling the appearance of superconductivity in Ta₂PdSe₆. Furthermore, the superconductivity is very robust up to 62.6 GPa, the highest pressure conducted in this study. The pressure evolution of the transport property and the emergent superconductivity are reproducible in run 2, as shown in Fig. S2. The arrows indicate the onset of the superconducting transition. A slight upturn of resistance preceding the superconducting transition could be ascribed to the pressure inhomogeneity or pressure induced disorder.

To understand the pressure evolution of transport properties in Ta₂PdSe₆, high-pressure magnetoresistance ($\text{MR} = [(\rho_{xx}(H) - \rho_{xx}(0)) / \rho_{xx}(0)] \times 100\%$) and Hall resistivity ρ_{xy} measurements were further conducted. Figure 3 shows the pressure-evolution of MR and Hall resistivity curves $\rho_{xy}(H)$ at 10 K under various pressures. These curves are plotted by the symmetric and anti-symmetric analyses, respectively, as shown in supplementary Fig. S3. Notably, the MR is strikingly suppressed with increasing pressure and is less than 1% above 18.3 GPa, which is comparable to Nb₂Pd_xSe₅ superconductor (less than 2% at 10 K) [7], as shown in the inset of Fig. 3(a). While the superconductivity is detected at 18.3 GPa, the MR effect becomes negligible in Ta₂PdSe₆. Note that the Weyl semimetal WTe₂ with large MR at ambient pressure becomes a superconductor at ~ 5 GPa, accompanied by the dramatically suppressed MR [38,39], which is quite similar to the case of pressurized Ta₂PdSe₆. As shown in

Fig. 3(b), the $\rho_{xy}(H)$ curve exhibits a nonlinear behavior with positive slope at 1.0 GPa, indicating a hole-dominated multiband feature. The slope of $\rho_{xy}(H)$ decreases monotonically with increasing pressure. At 15.3 GPa, the $\rho_{xy}(H)$ curve becomes to be linear in the whole field region. Further increase of the pressure above the critical pressure $P_c \sim 18.3$ GPa lead to the slope of $\rho_{xy}(H)$ changing from positive to negative. The sign reversal of the Hall resistivity around the pressure when the superconductivity starting to be observed is also reproducible in run 2 [see Fig. S4], demonstrates a crossover of the dominant carrier type concomitant with the emergent superconductivity. We noted that the electron-dominated behavior observed in pressurized Ta₂PdSe₆ (above P_c) is similar to the case of Nb₂PdS₅ [40] and Nb₂Pd_xSe₅ [7] superconductors.

The effect of the external magnetic field on superconductivity of pressurized Ta₂PdSe₆ was investigated in run 3. As shown in Fig. 4(a), when the temperature cooled down to 0.5 K, the zero-resistance state was observed at 17.7 GPa, signaling the appearance of superconductivity in Ta₂PdSe₆. The T_c^{zero} is enhanced monotonously with increasing pressure. As seen in Fig. 4(b), the superconducting transition is gradually suppressed with increasing magnetic field. To determine the upper critical field $\mu_0 H_{c2}(0)$, we chose a resistance criterion of $R_{\text{cri}} = 90\%R_n$ (R_n is the normal state resistance) and plotted the temperature dependence of $\mu_0 H_{c2}$ in Fig. 4(d). The Werthamer–Helfand–Hohenberg (WHH) model was used to fit the data [41]. The estimated $\mu_0 H_{c2}(0) \sim 2.1$ T is much lower than the weak-coupling Pauli limit $\mu_0 H_P(0) = 1.84T_c$ (~ 3.8 T), which suggests the absence of Pauli paramagnetic pair-breaking effect. According to the relationship $\mu_0 H_{c2} = \Phi_0/(2\pi\xi^2)$, where $\Phi_0 = 2.07 \times 10^{-15}$ Wb is the flux quantum, the coherence length $\xi_{\text{GL}}(0)$ of 125.5 Å is obtained. Similar analyses were applied to the case of 39.7 GPa. The obtained $\mu_0 H_{c2}(0)$ and $\xi_{\text{GL}}(0)$ are 2.7 T and 110.7 Å, respectively. In contrast with Ta₂PdSe₆, the ratio of $\mu_0 H_{c2}(0)/T_c$ were about 5.6-6.2 in M₂Pd_xX₅ (M = Nb, Ta; X = S, Se) superconductors, much larger than that of Pauli limit ~ 1.84 [6-9]. The significant difference in the upper critical field value suggested that the superconducting mechanism is likely different in superconducting Ta₂PdSe₆ and M₂Pd_xX₅.

To clarify the relationship between the emergent superconductivity and crystal structure in pressurized Ta₂PdSe₆, we further performed high-pressure synchrotron XRD experiments. As shown in Fig. 5(a), all the XRD peaks continuously shift towards higher angles without appearance of new peaks up to 36.2 GPa. Using the Le Bail

method, the XRD patterns at each pressure can be indexed with the monoclinic $C2/m$ structure at ambient pressure [21]. Note that the strongest peak is (111), rather than $(20\bar{1})$ from the calculated XRD pattern, as shown in Fig. S5. The different relative strength of the XRD peaks between the experiment and calculation could be ascribed to the preferred orientation in pressurized Ta_2PdSe_6 powder. Typical analysis of the XRD patterns at 0.4, 11.2, 21.8, and 30.5 GPa are shown in supplementary Fig. S6. We extract the lattice parameters as a function of pressure, as shown in Fig. 5(b) and supplementary Table 1. The pressure dependent volume is depicted in Fig. 5(c). By the fitting of the third-order Birch-Murnaghan equation of state [42], we obtained the ambient pressure volume $V_0 = 391.1 \pm 1.8 \text{ \AA}^3$, bulk modulus $B_0 = 50.5 \pm 4.7 \text{ GPa}$, and its first pressure derivative $B_0' = 8.4 \pm 0.2$, respectively. Moreover, we examined the phonon stability of the $C2/m$ structure under pressure. As shown in supplementary Fig. S7, Ta_2PdSe_6 is dynamically stable under pressure up to 40 GPa in the monoclinic structure. These results indicate no structure phase transition under pressure, thus ruling out the structural origin of the pressure-induced superconductivity in Ta_2PdSe_6 .

To have a comprehensive understanding of the superconductivity in the pressurized Ta_2PdSe_6 , we constructed a phase diagram in Fig. 6. There are two distinct regions separated by a critical pressure $P_c \sim 18.3 \text{ GPa}$, *i.e.*, the semimetallic state with MR and the superconducting state. It is clear that the appearance of superconductivity is accompanied by unusual evolution of the transport properties, including the dramatically suppressed MR, abrupt enhancement of resistance at 10 K, and sign change of the Hall coefficient R_H [see Fig. 6(b)]. With increasing pressure, it is rare to observe concurrently the large change in the MR, Hall coefficient and resistance of a common compound. Without detecting a structural transition, the simultaneously occurrence of anomalies in the transport properties is reminiscent of a Lifshitz transition [43-50]. Such transition is a peculiar "electron transition" due to variation of the topology of the Fermi surface during its continuous deformation at high pressures [43]. Especially, the sign reversal of the R_H indicates that the hole-dominated transport behavior maintains up to 18.3 GPa and transforms into electron-dominated behavior at higher pressures, which could be viewed as a signature of a modification of the Fermi surface. We note that the reported Lifshitz transitions in $ZrTe_5$ and $NiTe_2$ also involve the change of charge carrier type [44,45], which are very similar to our case. As shown in Fig. 6(a), upon compression, the T_c^{zero} of the pressurized Ta_2PdSe_6 increases and the

superconductivity is robust up to 62.6 GPa, in contrast to a dome-shaped phase diagram in quasi-1D Ta₄Pd₃Te₁₆ due to the competition between CDW and superconductivity [19,20].

Furthermore, we calculated pressure-dependent GGA+MBJ+SOC band structures at 0, 10, 20, 30, and 40 GPa, and the results are shown in Fig. 7. In the case of pressurized Ta₂PdSe₆, Fermi surface topology has relatively large changes along with the increment of pressure. Two significant evolutions are found in the electronic band structure. First, three conduction bands around I|I₁, X₁|X, and N|M points are downshifted below the Fermi Level starting from 10 GPa, leading to a Lifshitz transition for the Fermi surface topology (Fig. 7(b-e)). Second, a valence band (marked by a black arrow) around Γ -point is lifted above the Fermi Level at 20 GPa (Fig. 7(c-e)), demonstrating a Lifshitz transition associated with the change of the Fermi surface topology around Γ -point. The Lifshitz transition could be a driven force for the appearance of superconductivity in pressurized Ta₂PdSe₆. Pressure-induced superconductivity has been associated with the Lifshitz transition in the systems such as the iron-based superconductors, black phosphorus, PtTe₂, and topological kagome metal Cs₃VSb₅ when there exists no structural phase transition [46-50]. For instance, it is observed that superconductivity reemerges at 5 GPa in FeS superconductor [46], which is theoretically ascribed to a Lifshitz transition [47].

IV. CONCLUSIONS

In conclusion, we have systematically investigated the pressure effect on the structural and electronic properties of quasi-1D semimetal Ta₂PdSe₆. We observed a superconducting transition above the critical pressure $P_c \sim 18.3$ GPa. In contrast to isostructural Ta₂PdSe₅, we found the absence of Pauli paramagnetic pair-breaking effect in the pressurized Ta₂PdSe₆. Despite of the robust pristine monoclinic structure under pressure, abnormal evolutions of transport properties occur concurrently around P_c , implying an electronic origin of the emergent superconductivity. We hope our results will stimulate further theoretical work to address the nature of the superconductivity in Ta₂PdSe₆.

ACKNOWLEDGMENTS

The authors gratefully acknowledge financial support from the National Key Research and Development Program of China (Grant Nos. 2018YFA0305700, 2021YFA1600204), the National Natural Science Foundation of China (Grant Nos. U1932152, 11874362, 12174395, 12004004, 11704387, U19A2093, U1832209, and 12174397), the Natural Science Foundation of Anhui Province (Grant Nos. 1808085MA06, 2008085QA40, and 1908085QA18), the Users with Excellence Project of Hefei Center CAS (Grant Nos. 2021HSC-UE008 and 2020HSC-UE015), the Collaborative Innovation Program of Hefei Science Center CAS (Grant No. 2020HSC-CIP014). A portion of this work was supported by the High Magnetic Field Laboratory of Anhui Province under Contract Nos. AHHM-FX-2020-02 and AHHM-FX-2021-03. Yonghui Zhou was supported by the Youth Innovation Promotion Association CAS (Grant No. 2020443). The high-pressure synchrotron X-ray diffraction experiments were performed at the beamline BL15U1, Shanghai Synchrotron Radiation Facility.

References

- [1] S. Manzeli, D. Ovchinnikov, D. Pasquier, O. V. Yazyev, and A. Kis, 2D transition metal dichalcogenides, *Nat. Rev. Mater.* **2**, 17033 (2017). <https://doi.org/10.1038/natrevmats.2017.33>
- [2] J. R. Schaibley, H. Yu, G. Clark, P. Rivera, J. S. Ross, K. L. Seyler, W. Yao, and X. Xu, Valleytronics in 2D materials, *Nat. Rev. Mater.* **1**, 16055 (2016). <https://doi.org/10.1038/natrevmats.2016.55>
- [3] K. S. Novoselov, A. Mishchenko, A. Carvalho, and A. H. Castro Neto, 2D materials and van der Waals heterostructures, *Science* **353**, aac9439 (2016). <https://doi.org/10.1126/science.aac9439>
- [4] Q. H. Wang, K. Kalantar-Zadeh, A. Kis, J. N. Coleman, and M. S. Strano, Electronics and optoelectronics of two-dimensional transition metal dichalcogenides, *Nat. Nanotechnol.* **7**, 699 (2012). <https://doi.org/10.1038/nnano.2012.193>
- [5] X. Xu, W. Yao, D. Xiao, and T. F. Heinz, Spin and pseudospins in layered transition metal dichalcogenides, *Nat. Phys.* **10**, 343 (2014). <https://doi.org/10.1038/nphys2942>
- [6] Q. Zhang, G. Li, D. Rhodes, A. Kiswandhi, T. Besara, B. Zeng, J. Sun, T. Siegrist, M. D. Johannes, and L. Balicas, Superconductivity with extremely large upper critical fields in $\text{Nb}_2\text{Pd}_{0.81}\text{S}_5$, *Sci. Rep.* **3**, 1446 (2013). <https://doi.org/10.1038/srep01682>
- [7] S. Khim, B. Lee, K.-Y. Choi, B.-G. Jeon, D. H. Jang, D. Patil, S. Patil, R. Kim, E. S. Choi, S. Lee, J. Yu, and K. H. Kim, Enhanced upper critical fields in a new quasi-one-dimensional superconductor $\text{Nb}_2\text{Pd}_x\text{Se}_5$, *New J. Phys.* **15**, 123031 (2013). <https://doi.org/10.1088/1367-2630/15/12/123031>
- [8] Y. Lu, T. Takayama, A. F. Bangura, Y. Katsura, D. Hashizume, and H. Takagi, Superconductivity at 6 K and the Violation of Pauli Limit in $\text{Ta}_2\text{Pd}_x\text{S}_5$, *J. Phys. Soc. Jpn.* **83**, 023702 (2014). <https://doi.org/10.7566/JPSJ.83.023702>
- [9] J. Zhang, J. K. Dong, Y. Xu, J. Pan, L. P. He, L. J. Zhang, and S. Y. Li, Superconductivity at 2.5 K in the new transition-metal chalcogenide Ta_2PdSe_5 , *Supercond. Sci. Technol.* **28**, 115015 (2015). <https://doi.org/10.1088/0953-2048/28/11/115015>
- [10] C. Q. Niu, J. H. Yang, Y. K. Li, B. Chen, N. Zhou, J. Chen, L. L. Jiang, B. Chen, X. X. Yang, C. Cao, J. Dai, and X. Xu, Effect of selenium doping on the superconductivity of $\text{Nb}_2\text{Pd}(\text{S}_{1-x}\text{Se}_x)_5$, *Phys. Rev. B* **88**, 104507 (2013). <https://doi.org/10.1103/PhysRevB.88.104507>
- [11] N. Zhou, X. Xu, J. R. Wang, J. H. Yang, Y. K. Li, Y. Guo, W. Z. Yang, C. Q. Niu, B. Chen, C. Cao, and J. Dai, Controllable spin-orbit coupling and its influence on the upper critical field in the chemically doped quasi-one-dimensional Nb_2PdS_5 superconductor, *Phys. Rev. B* **90**, 094520 (2014). <https://doi.org/10.1103/PhysRevB.90.094520>
- [12] H. Yu, M. Zuo, L. Zhang, S. Tan, C. Zhang, and Y. Zhang, Superconducting fiber with transition temperature up to 7.43 K in $\text{Nb}_2\text{Pd}_x\text{S}_{5-x}$ ($0.6 < x < 1$), *J. Am. Chem. Soc.* **135**, 12987 (2013). <https://doi.org/10.1021/ja4062079>

- [13] W. Ning, H. Yu, Y. Liu, Y. Han, N. Wang, J. Yang, H. Du, C. Zhang, Z. Mao, Y. Liu, M. Tian, and Y. Zhang, Superconductor-insulator transition in quasi-one-dimensional single-crystal Nb₂PdS₅ nanowires, *Nano Lett.* **15**, 869 (2015). <https://doi.org/10.1021/nl503538s>
- [14] L. Bao, Y. Bi, X. Liu, X. Yang, T. Hao, S. Tian, Z. Wang, J. Li, and C. Gu, Thickness dependence of superconductivity in single-crystal Ta₄Pd₃Te₁₆ nanoribbons, *Appl. Phys. Lett.* **113**, 022603 (2018). <https://doi.org/10.1063/1.5040046>
- [15] E. Zhang, X. Xu, C. Huang, Y. C. Zou, L. Ai, S. Liu, P. Leng, Z. Jia, Y. Zhang, M. Zhao, Z. Li, Y. Yang, J. Liu, S. J. Haigh, Z. Mao, and F. Xiu, Magnetic-Field-Induced Re-entrance of Superconductivity in Ta₂PdS₅ Nanostrips, *Nano Lett.* **21**, 288 (2021). <https://doi.org/10.1021/acs.nanolett.0c03655>
- [16] Q. Fan, W. H. Zhang, X. Liu, Y. J. Yan, M. Q. Ren, M. Xia, H. Y. Chen, D. F. Xu, Z. R. Ye, W. H. Jiao, G. H. Cao, B. P. Xie, T. Zhang, and D. L. Feng, Scanning tunneling microscopy study of superconductivity, magnetic vortices, and possible charge-density wave in Ta₄Pd₃Te₁₆, *Phys. Rev. B* **91**, 104506 (2015). <https://doi.org/10.1103/PhysRevB.91.104506>
- [17] Z. Li, W. H. Jiao, G. H. Cao, and G.-q. Zheng, Charge fluctuations and nodeless superconductivity in quasi-one-dimensional Ta₄Pd₃Te₁₆ revealed by Te₁₂₅-NMR and Ta₁₈₁-NQR, *Phys. Rev. B* **94**, 174511 (2016). <https://doi.org/10.1103/PhysRevB.94.174511>
- [18] T. Helm, F. Flicker, R. Kealhofer, P. J. W. Moll, I. M. Hayes, N. P. Breznay, Z. Li, S. G. Louie, Q. R. Zhang, L. Balicas, J. E. Moore, and J. G. Analytis, Thermodynamic anomaly above the superconducting critical temperature in the quasi-one-dimensional superconductor Ta₄Pd₃Te₁₆, *Phys. Rev. B* **95**, 075121 (2017). <https://doi.org/10.1103/PhysRevB.95.075121>
- [19] J. Pan, W. H. Jiao, X. C. Hong, Z. Zhang, L. P. He, P. L. Cai, J. Zhang, G. H. Cao, and S. Y. Li, Nodal superconductivity and superconducting dome in the layered superconductor Ta₄Pd₃Te₁₆, *Phys. Rev. B* **92**, 180505(R) (2015). <https://doi.org/10.1103/PhysRevB.92.180505>
- [20] Z. Shi, S. J. Kuhn, F. Flicker, T. Helm, J. Lee, W. Steinhardt, S. Dissanayake, D. Graf, J. Ruff, G. Fabbris, D. Haskel, and S. Haravifard, Incommensurate two-dimensional checkerboard charge density wave in the low-dimensional superconductor Ta₄Pd₃Te₁₆, *Phys. Rev. Res.* **2**, 042042(R) (2020). <https://doi.org/10.1103/PhysRevResearch.2.042042>
- [21] A. K. Douglas, J. S. Philip, N. E. B., J. A. I., S. M. Y., and L. J. X., New Layered Ternary Chalcogenides: Ta₂PdS₆, Ta₂PdSe₆, Nb₂PdS₆, Nb₂PdSe₆, *Inorg. Chem.* **24**, 3063 (1985). <https://doi.org/10.1021/ic00213a038>
- [22] B. Tiwari, B. B. Prasad, R. Jha, D. K. Singh, and V. P. S. Awana, Superconductivity at 4 K in Pd-Deficient Layered Ta₂Pd_xS₆, *J. Supercond. Nov. Magn.* **27**, 2181 (2014). <https://doi.org/10.1007/s10948-014-2631-z>
- [23] S. Nakamura, T. Noji, T. Hatakeda, K. Sato, T. Kawamata, M. Kato, and Y. Koike, New ethylenediamine-intercalated superconductor (C₂H₈N₂)_yTa₂PdSe₆ with T_c = 4.5 K, *J. Phys.: Conf. Ser.* **969**, 012076 (2018). <https://doi.org/10.1088/1742-6596/969/1/012076>

- [24] P. Yu, Q. Zeng, C. Zhu, L. Zhou, W. Zhao, J. Tong, Z. Liu, and G. Yang, Ternary Ta₂PdS₆ Atomic Layers for an Ultrahigh Broadband Photoresponsive Phototransistor, *Adv. Mater.* **33**, 2005607 (2021). <https://doi.org/10.1002/adma.202005607>
- [25] A. Nakano, U. Maruoka, F. Kato, H. Taniguchi, and I. Terasaki, Room Temperature Thermoelectric Properties of Isostructural Selenides Ta₂PdS₆ and Ta₂PdSe₆, *J. Phys. Soc. Jpn.* **90**, 033702 (2021). <https://doi.org/10.7566/JPSJ.90.033702>
- [26] A. Nakano, A. Yamakage, U. Maruoka, H. Taniguchi, Y. Yasui, and I. Terasaki, Giant Peltier conductivity in an uncompensated semimetal Ta₂PdSe₆, *J. Phys. Energy* **3**, 044004 (2021). <https://doi.org/10.1088/2515-7655/ac2357>
- [27] T. Zhang, Y. Jiang, Z. Song, H. Huang, Y. He, Z. Fang, H. Weng, and C. Fang, Catalogue of topological electronic materials, *Nature* **566**, 475 (2019). <https://doi.org/10.1038/s41586-019-0944-6>
- [28] C. Prescher and V. B. Prakapenka, DIOPTAS: a program for reduction of two-dimensional X-ray diffraction data and data exploration, *High Press. Res.* **35**, 223 (2015). <https://doi.org/10.1080/08957959.2015.1059835>
- [29] B. A. Hunter, Rietica-A Visual Rietveld Program, International Union of Crystallography Commission on Powder Diffraction Newsletter No. 20 (Summer, 1998), <http://www.rietica.org>.
- [30] H. K. Mao, J. Xu, and P. M. Bell, Calibration of the ruby pressure gauge to 800 kbar under quasi-hydrostatic conditions, *J. Geophys. Res.* **91**, 4673 (1986). <https://doi.org/10.1029/JB091iB05p04673>
- [31] G. Kresse and J. Hafner, Ab initio molecular dynamics for liquid metals, *Phys. Rev. B* **47**, 558 (1993). <https://doi.org/10.1103/PhysRevB.47.558>
- [32] G. Kresse and J. Furthmuller, Efficient iterative schemes for ab initio total-energy calculations using a plane-wave basis set, *Phys. Rev. B* **54**, 11169 (1996). <https://doi.org/10.1103/PhysRevB.54.11169>
- [33] J. P. Perdew, K. Burke, and M. Ernzerhof, Generalized Gradient Approximation Made Simple, *Phys. Rev. Lett.* **77**, 3865 (1996). <https://doi.org/10.1103/PhysRevLett.77.3865>
- [34] F. Tran and P. Blaha, Accurate band gaps of semiconductors and insulators with a semilocal exchange-correlation potential, *Phys. Rev. Lett.* **102**, 226401 (2009). <https://doi.org/10.1103/PhysRevLett.102.226401>
- [35] G. Kresse and D. Joubert, From ultrasoft pseudopotentials to the projector augmented-wave method, *Phys. Rev. B* **59**, 1758 (1999). <https://doi.org/10.1103/PhysRevB.59.1758>
- [36] P. E. Blochl, Projector augmented-wave method, *Phys. Rev. B* **50**, 17953 (1994). <http://doi.org/10.1103/PhysRevB.50.17953>
- [37] A. Togo and I. Tanaka, First principles phonon calculations in materials science, *Scr. Mater.* **108**, 1 (2015). <https://doi.org/10.1016/j.scriptamat.2015.07.021>
- [38] D. Kang, Y. Zhou, W. Yi, C. Yang, J. Guo, Y. Shi, S. Zhang, Z. Wang, C. Zhang, S. Jiang, A. Li, K. Yang, Q. Wu, G. Zhang, L. Sun, and Z. Zhao, Superconductivity emerging from

- a suppressed large magnetoresistant state in tungsten ditelluride, *Nat. Commun.* **6**, 7804 (2015). <https://doi.org/10.1038/ncomms8804>
- [39] X. C. Pan, X. Chen, H. Liu, Y. Feng, Z. Wei, Y. Zhou, Z. Chi, L. Pi, F. Yen, F. Song, X. Wan, Z. Yang, B. Wang, G. Wang, and Y. Zhang, Pressure-driven dome-shaped superconductivity and electronic structural evolution in tungsten ditelluride, *Nat. Commun.* **6**, 7805 (2015). <https://doi.org/10.1038/ncomms8805>
- [40] Q. Chen, X. Yang, X. Yang, J. Chen, C. Shen, P. Zhang, Y. Li, Q. Tao, and Z.-A. Xu, Enhanced superconductivity in hole-doped Nb₂PdS₅, *Front. Phys.* **12**, 127402 (2016). <https://doi.org/10.1007/s11467-016-0637-7>
- [41] N. R. Werthamer, E. Helfand, and P. C. Hohenberg, Temperature and Purity Dependence of the Superconducting Critical Field, H_{c2}. III. Electron Spin and Spin-Orbit Effects, *Phys. Rev.* **147**, 295 (1966). <https://doi.org/10.1103/PhysRev.147.295>
- [42] F. Birch, Finite Elastic Strain of Cubic Crystals, *Phys. Rev.* **71**, 809 (1947). <https://doi.org/10.1103/PhysRev.71.809>
- [43] I. M. Lifshitz, Anomalies of electron characteristics of a metal in the high pressure region, *Zh. Eksp. Teor. Fiz.* **38**, 1569 (1960).
- [44] H. Chi, C. Zhang, G. Gu, D. E. Kharzeev, X. Dai, and Q. Li, Lifshitz transition mediated electronic transport anomaly in bulk ZrTe₅, *New J. Phys.* **19**, 015005 (2017). <https://doi.org/10.1088/1367-2630/aa55a3>
- [45] M. Qi, C. An, Y. Zhou, H. Wu, B. Zhang, C. Chen, Y. Yuan, S. Wang, Y. Zhou, X. Chen, R. Zhang, and Z. Yang, Pressure-driven Lifshitz transition in type-II Dirac semimetal NiTe₂, *Phys. Rev. B* **101**, 115124 (2020). <https://doi.org/10.1103/PhysRevB.101.115124>
- [46] X. Lai, Y. Liu, X. Lu, S. Zhang, K. Bu, C. Jin, H. Zhang, J. Lin, and F. Huang, Suppression of superconductivity and structural phase transitions under pressure in tetragonal FeS, *Sci. Rep.* **6**, 31077 (2016). <https://doi.org/10.1038/srep31077>
- [47] M. Shimizu, N. Takemori, D. Guterding, and H. O. Jeschke, Two-Dome Superconductivity in FeS Induced by a Lifshitz Transition, *Phys. Rev. Lett.* **121**, 137001 (2018). <https://doi.org/10.1103/PhysRevLett.121.137001>
- [48] J. Guo, H. Wang, F. von Rohr, W. Yi, Y. Zhou, Z. Wang, S. Cai, S. Zhang, X. Li, Y. Li, J. Liu, K. Yang, A. Li, S. Jiang, Q. Wu, T. Xiang, R. J. Cava, and L. Sun, Electron-hole balance and the anomalous pressure-dependent superconductivity in black phosphorus, *Phys. Rev. B* **96**, 224513 (2017). <https://doi.org/10.1103/PhysRevB.96.224513>
- [49] Z. Zhang, Z. Chen, Y. Zhou, Y. Yuan, S. Wang, J. Wang, H. Yang, C. An, L. Zhang, X. Zhu, Y. Zhou, X. Chen, J. Zhou, and Z. Yang, Pressure-induced reemergence of superconductivity in the topological kagome metal CsV₃Sb₅, *Phys. Rev. B* **103**, 224513 (2021). <https://doi.org/10.1103/PhysRevB.103.224513>
- [50] F. Liu, J. Li, K. Zhang, S. Peng, H. Huang, M. Yan, N. Li, Q. Zhang, S. Guo, X. Lü, P. Cai, L. Yin, S. Zhou, W. Duan, J. Shen, and W. Yang, Pressure-induced Lifshitz transition in the type II Dirac semimetal PtTe₂, *Sci. China Phys. Mech. Astron.* **62**, 048211 (2018). <https://doi.org/10.1007/s11433-018-9319-3>

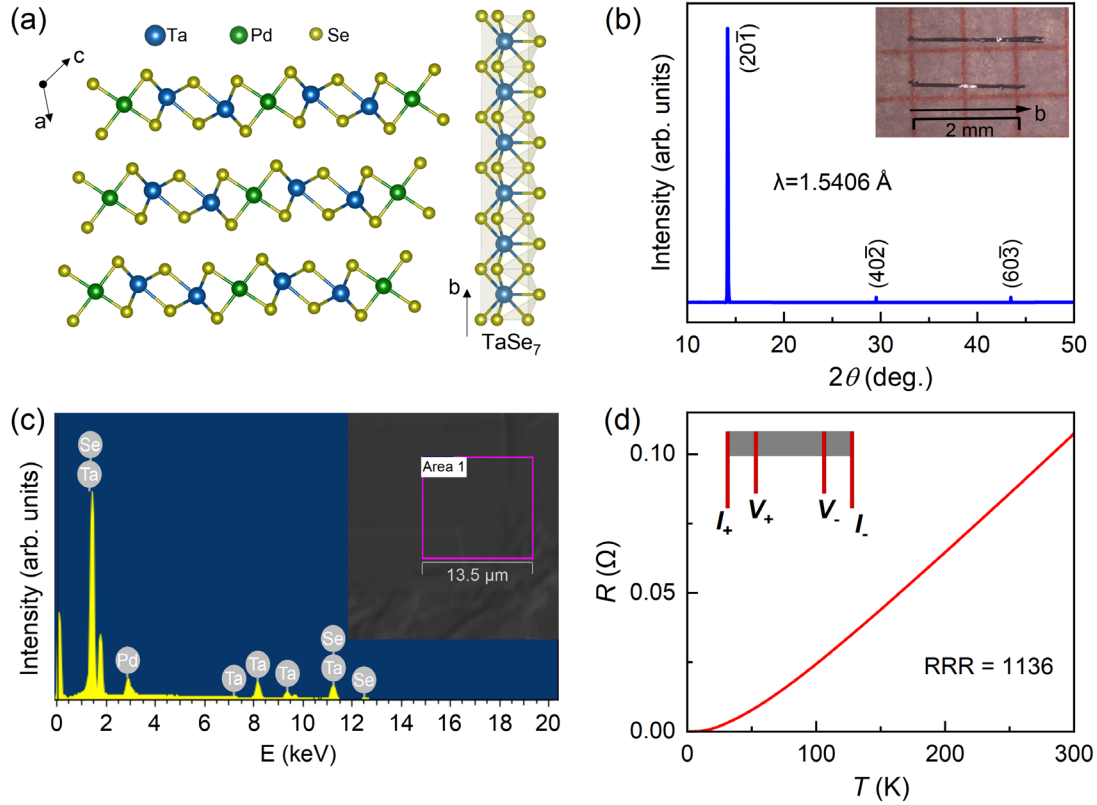


FIG. 1. (a) Schematic crystal structure of Ta_2PdSe_6 (monoclinic, space group $C2/m$). The blue, green, and orange spheres represent Ta, Pd, and Se, respectively. (b) XRD pattern of Ta_2PdSe_6 single crystal at room temperature ($\lambda = 1.5406 \text{ \AA}$). The inset shows a picture of as-grown single crystals. (c) Energy-dispersive X-ray spectroscopy of a piece of single crystal with area-scanning mode. (d) Temperature dependence of resistance of a piece of single crystal with a residual resistance ratio $\text{RRR} = 1136$ at ambient pressure. Inset: Schematic configuration of the four-probe electrical transport measurement.

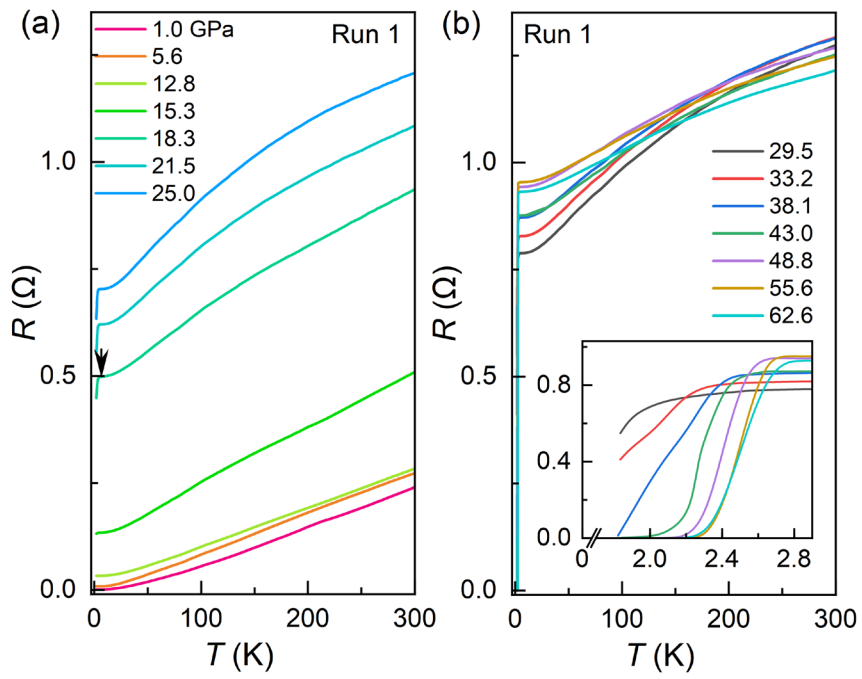


FIG. 2. Pressure evolution of resistance-temperature curves in Ta_2PdSe_6 . Inset of (b): Enlarged view of the low-temperature region in run 1.

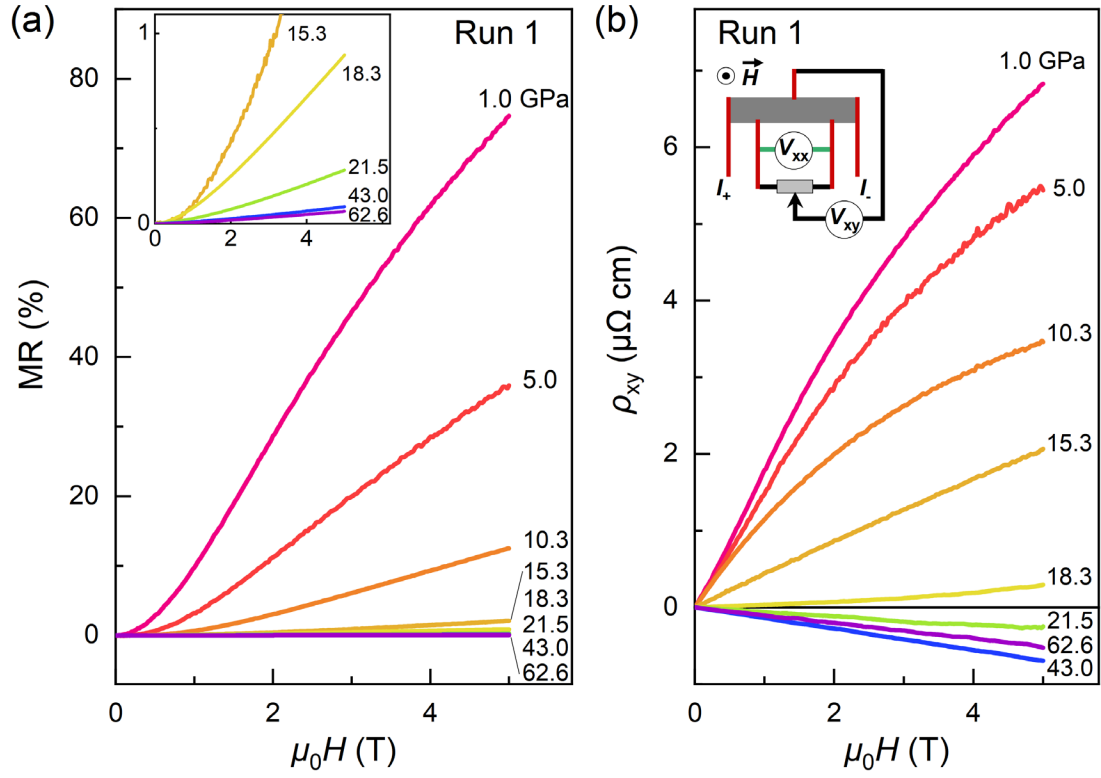


FIG. 3. (a) Pressure evolution of representative magnetoresistance curves in Ta₂PdSe₆ at 10 K. Inset: Enlarged view of the pressure above 15.3 GPa in run 1. (b) Pressure evolution of representative Hall resistivity curves $\rho_{xy}(H)$ in Ta₂PdSe₆ at 10 K. Inset: Schematic configuration of the electrical transport measurement with five probes.

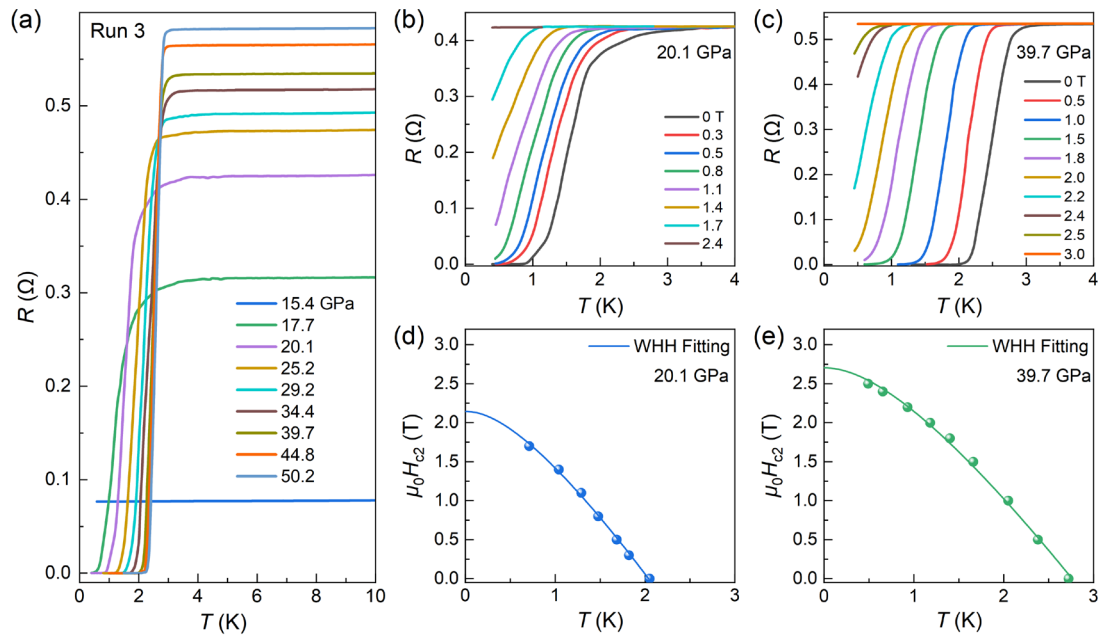


FIG. 4. Pressure evolution of resistance-temperature curves in run 3. (a) Enlarged view of the low-temperature region. Temperature-dependent resistance curves in Ta_2PdSe_6 under various magnetic fields at (b) 20.1 GPa and (d) 39.7 GPa in run 3. (c,e) Temperature dependence of the upper critical field $\mu_0 H_{c2}$. The solid lines represent the WWH fitting.

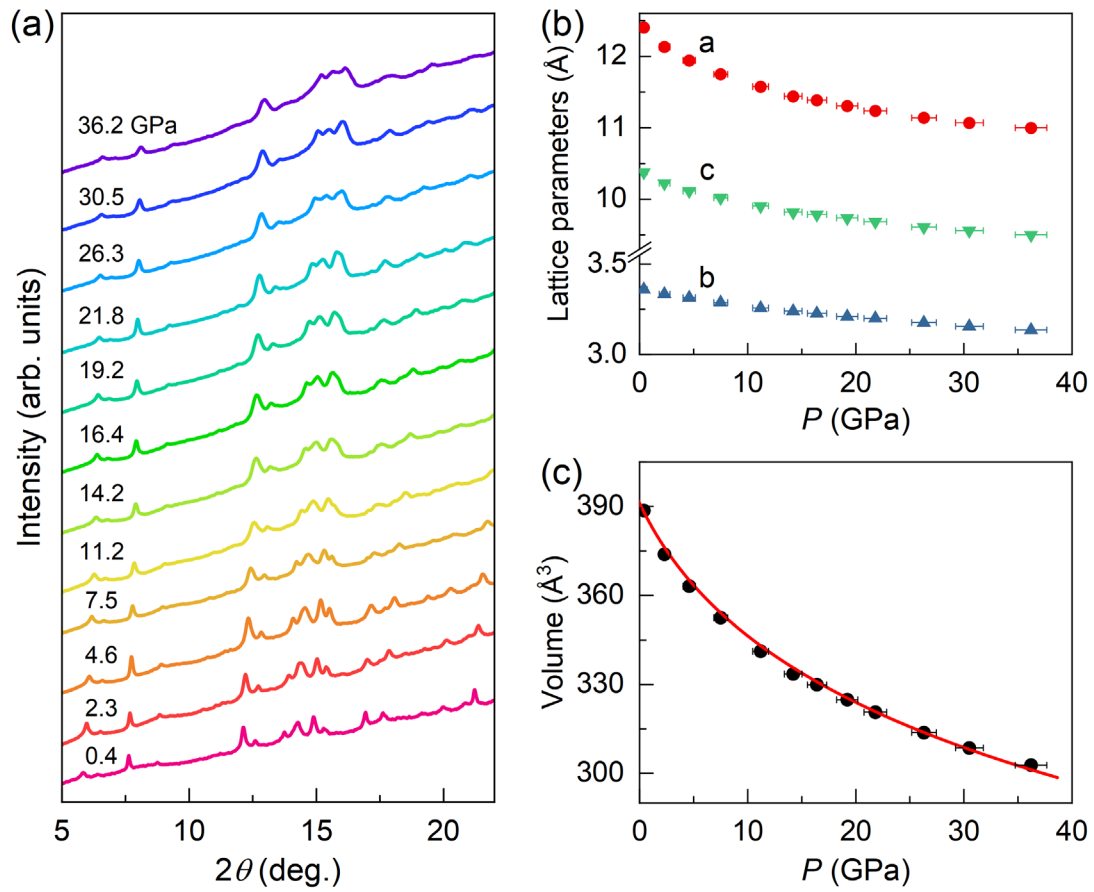


FIG. 5. (a) Pressure dependence of XRD patterns of Ta_2PdSe_6 at room temperature ($\lambda = 0.6199 \text{ \AA}$). (b) Lattice parameters a , b , and c as a function of pressure. (c) Volume-pressure phase diagram. The solid red line is fits based on the third-order Birch-Murnaghan equation of states.

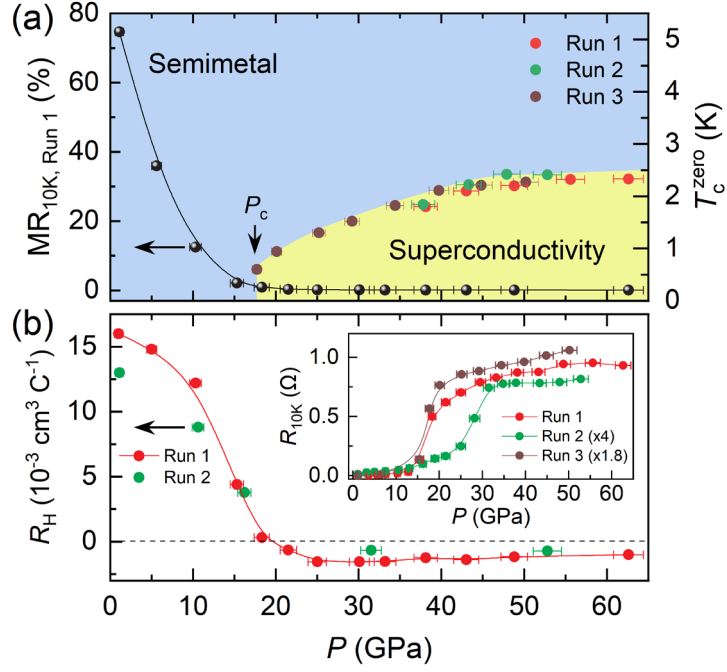


FIG. 6. Pressure–temperature phase diagram of Ta_2PdSe_6 and pressure-dependent Hall coefficient. (a) The red, green, and brown solid dots represent T_c^{zero} for run 1, run 2, and run 3, respectively. (b) Hall coefficient (R_H) as a function of pressure measured at 10 K and 5 T. Inset: Pressure-dependent resistance of Ta_2PdSe_6 at 10 K for three runs.

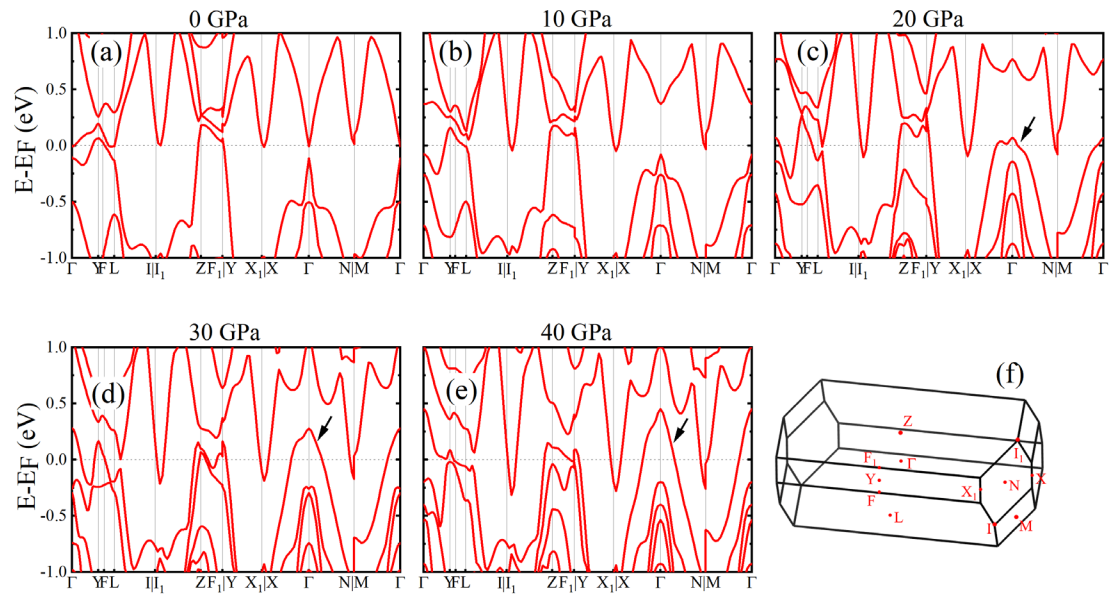


FIG. 7. (a)-(e) Calculated GGA+MBJ+SOC band structure at different pressure points (0, 10, 20, 30 and 40 GPa). Pressure dependent evolution of hole band pocket around Γ -point (marked by black arrow in (c)-(e)). (f) High symmetry points of the Brillouin zone.

Supplemental Material for

Pressure-induced superconductivity in quasi-one-dimensional semimetal



Haiyang Yang,^{1,2} Yonghui Zhou,^{1,*} Liangyu Li,^{1,2} Zheng Chen,^{1,2} Zhuyi Zhang,^{1,2}
Shuyang Wang,^{1,2} Jing Wang,^{1,2} Xuliang Chen,¹ Chao An,³ Ying Zhou,³ Min Zhang,³
Ranran Zhang,¹ Xiangde Zhu,¹ Lili Zhang,⁴ Xiaoping Yang,^{1,*} and Zhaorong Yang^{1,3,*}

¹*Anhui Key Laboratory of Condensed Matter Physics at Extreme Conditions, High Magnetic Field Laboratory, HFIPS, Chinese Academy of Sciences, Hefei 230031, China*

²*Science Island Branch of Graduate School, University of Science and Technology of China, Hefei 230026, China*

³*Institutes of Physical Science and Information Technology, Anhui University, Hefei 230601, China*

⁴*Shanghai Synchrotron Radiation Facility, Shanghai Advanced Research Institute, Chinese Academy of Sciences, Shanghai 201204, China*

*Corresponding authors.

yhzhou@hmfl.ac.cn;

xpyang@hmfl.ac.cn;

zryang@issp.ac.cn

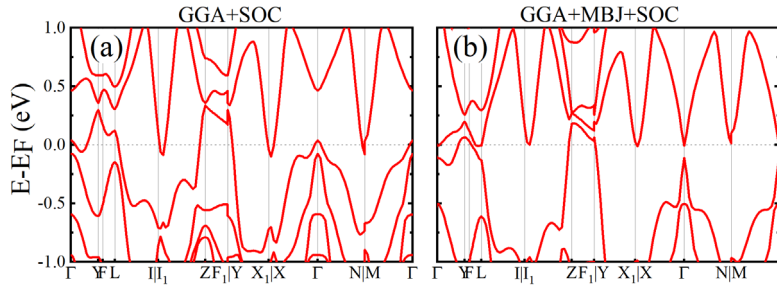


Fig. S1 (a,b) Calculated GGA+SOC and GGA+MBJ+SOC band structure at 0 GPa.

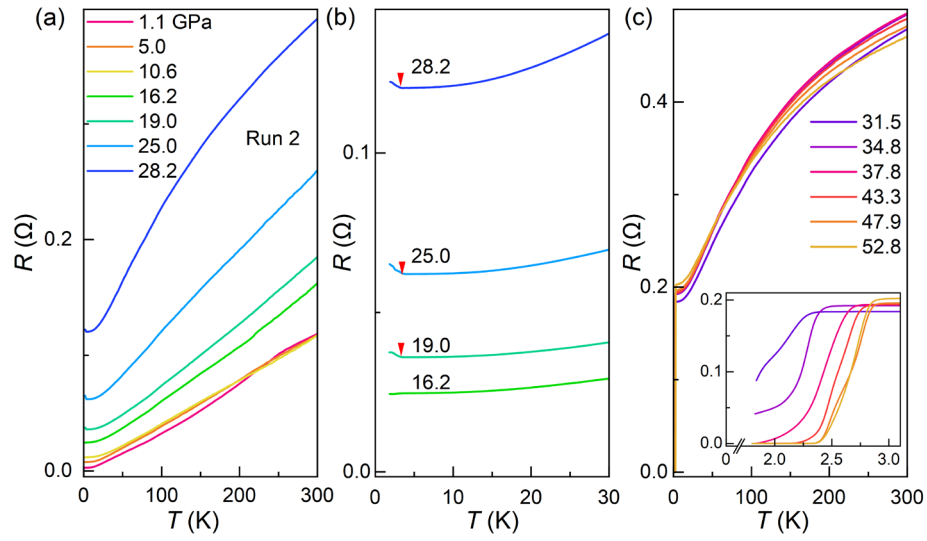


FIG. S2. Pressure evolution of resistance-temperature curves in Ta_2PdSe_6 in run 2. The arrows in (b) indicates the onset of the superconducting transition. Inset of (c): Enlarged view of the low-temperature region.

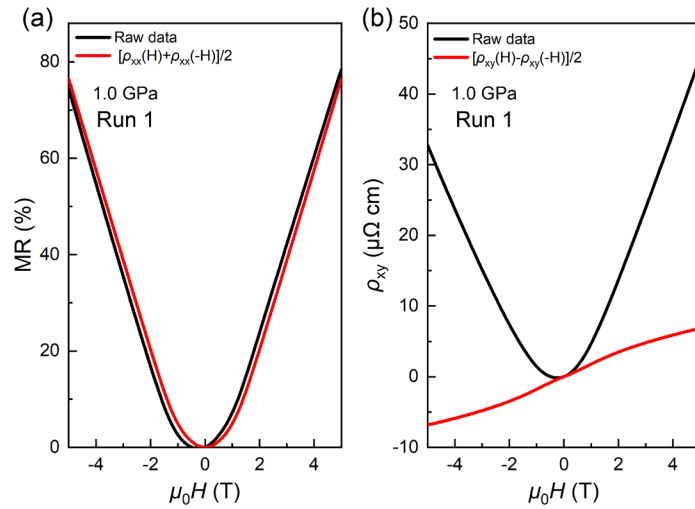


FIG. S3. Magnetoresistance ($\text{MR} = [\rho_{xx}(H) - \rho_{xx}(0)] / \rho_{xx}(0) \times 100\%$) and Hall resistivity curves at 10 K and 1.0 GPa in run 1 are plotted by the symmetric and anti-symmetric analyses, respectively.

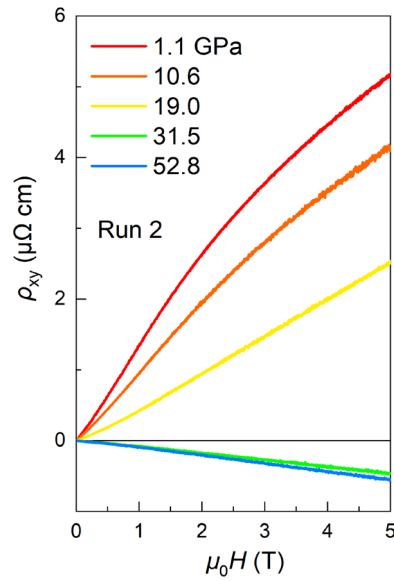


FIG. S4. Pressure evolution of representative Hall resistivity curves $\rho_{xy}(H)$ at 10 K in run 2.

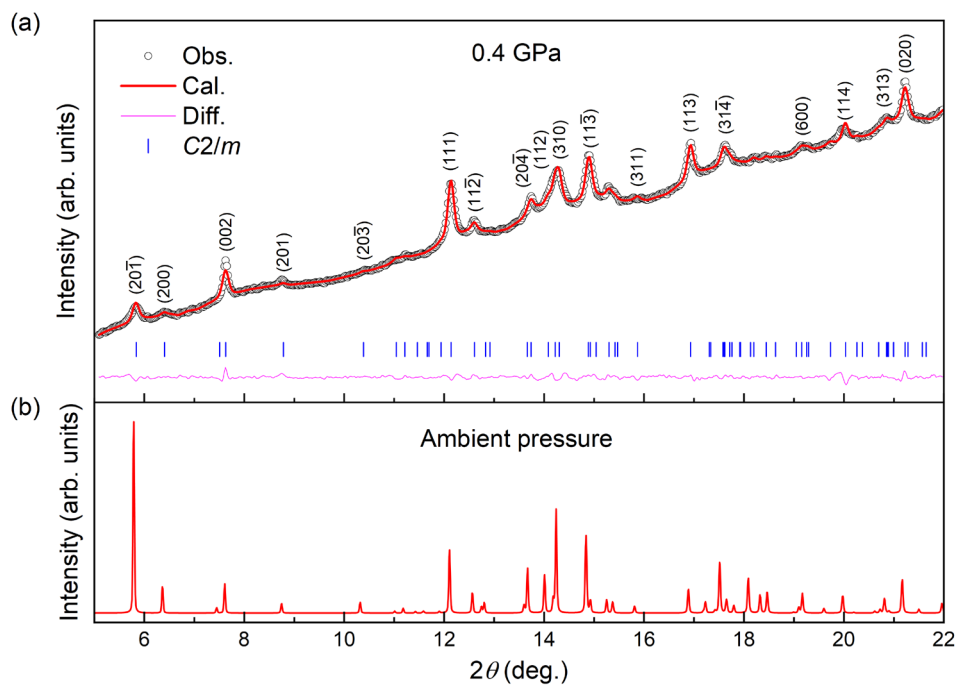


FIG. S5. (a) Representative Le Bail refinement of the XRD patterns at 0.4 GPa. The open circles and solid lines represent the observed and calculated data, respectively. The solid lines at the bottom denote the residual intensities. The vertical bars indicate the Bragg peak positions with monoclinic $C2/m$ phase. (b) The calculated XRD pattern at ambient pressure.

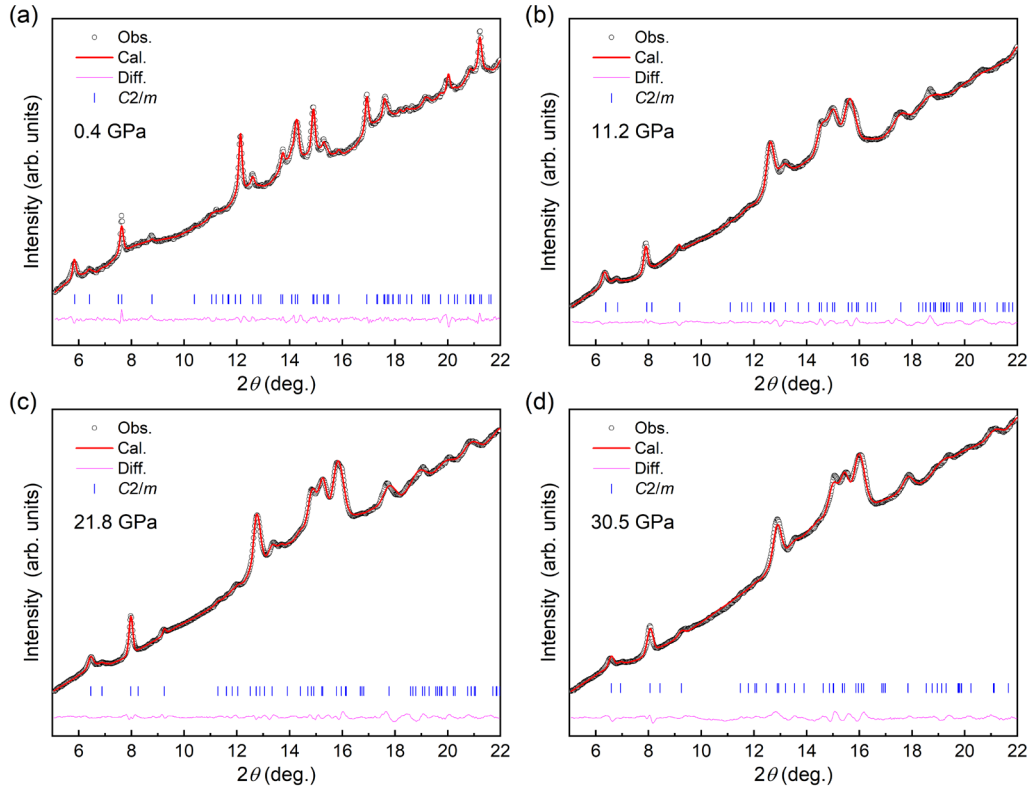


FIG. S6. Representative Le Bail refinements of the XRD patterns at 0.4, 11.2, 21.8, and 30.5 GPa, respectively. The open circles and solid lines represent the observed and calculated data, respectively. The solid lines at the bottom denote the residual intensities. The vertical bars indicate the Bragg peak positions with monoclinic $C2/m$ phase.

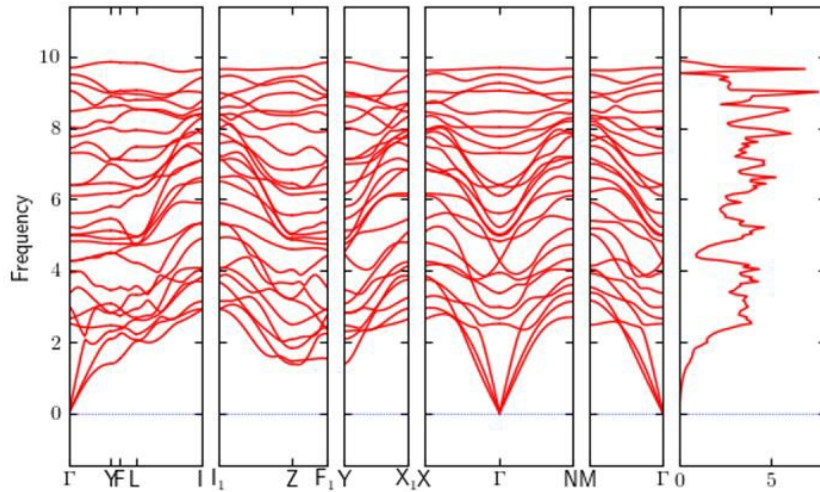


FIG. S7. The calculated phonon spectra of Ta_2PdSe_6 at 40 GPa.

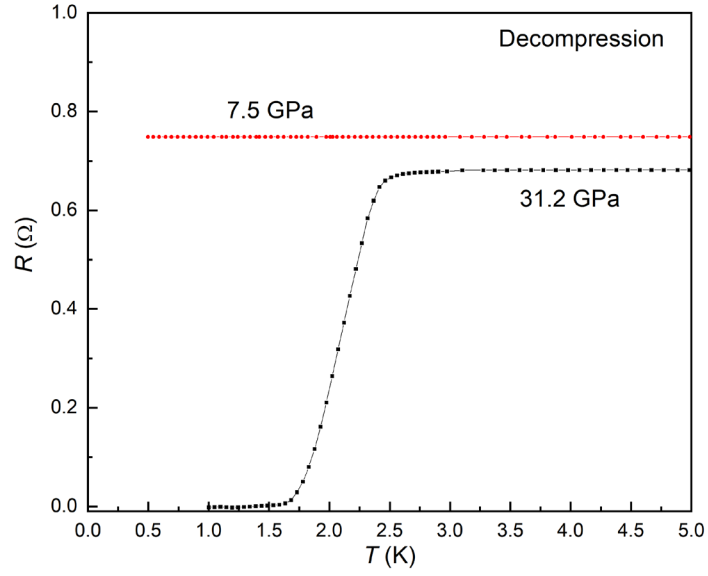


FIG. S8. $R(T)$ curve at 31.2 and 7.5 GPa during the decompression in run 3.

Table 1. The extracted lattice parameters as a function of pressure at room temperature.

$P(\text{GPa})$	$a(\text{\AA})$	$b(\text{\AA})$	$c(\text{\AA})$	$V(\text{\AA}^3)$	R_p	R_{wp}
0.4	12.402	3.360	10.377	388.624	0.7 %	1.3 %
2.3	12.131	3.334	10.224	373.916	0.6 %	1.2 %
4.6	11.939	3.314	10.117	363.159	0.7 %	1.4 %
7.5	11.748	3.288	10.018	352.51	0.6 %	1.1 %
11.2	11.573	3.256	9.903	341.196	0.6 %	0.9 %
14.2	11.437	3.240	9.817	333.546	0.6 %	1.0 %
16.4	11.384	3.226	9.785	329.908	0.6 %	1.2 %
19.2	11.303	3.210	9.737	324.836	0.5 %	1.1 %
21.8	11.236	3.199	9.686	320.649	0.7 %	1.2 %
26.3	11.138	3.176	9.611	313.784	0.5 %	1.0 %
30.5	11.067	3.156	9.558	308.551	0.6 %	0.8 %
36.2	10.996	3.134	9.498	302.780	0.6 %	1.1 %